

Unravelling Coherent Dynamics and Energy Dissipation in Photosynthetic Complexes by 2D Spectroscopy

Darius Abramavicius, Dmitri V. Voronine, and Shaul Mukamel

Natural Sciences, University of California, Irvine, California

ABSTRACT Spectroscopic studies of light harvesting and the subsequent energy conversion in photosynthesis can track quantum dynamics happening on the microscopic level. The Fenna-Matthews-Olson complex of the photosynthetic green sulfur bacteria *Chlorobium tepidum* is a prototype efficient light-harvesting antenna: it stores the captured photon energy in the form of excitons (collective excitations), which are subsequently converted to chemical energy with almost 100% efficiency. These excitons show an elaborate relaxation pattern involving coherent and incoherent pathways. We make use of the complex chirality and fundamental symmetries of multidimensional optical signals to design new sequences of ultrashort laser pulses that can distinguish between coherent quantum oscillations and incoherent energy dissipation during the exciton relaxation. The cooperative dynamical features, which reflect the coherent nature of excitations, are amplified. The extent of quantum oscillations and their timescales in photosynthesis can be readily extracted from the designed signals, showing that cooperativity is maintained during energy transport in the Fenna-Matthews-Olson complex. The proposed pulse sequences may also be applied to reveal information on the robustness of quantum states in the presence of fluctuating environments in other nanoscopic complexes and devices.

INTRODUCTION

Unraveling the energy transfer mechanisms in photosynthetic complexes from bacteria and higher plants is an important step toward the design of artificial light-harvesting and storing devices (1,2). The most studied complex—the Fenna-Matthews-Olson complex (FMO)—is a trimer of identical subunits, each consisting of seven bacteriochlorophyll (BChl) molecules embedded in a protein matrix as shown in Fig. 1 *a* (3). Its 2.1-Å resolution x-ray crystal structure reveals a chiral distribution of pigments in space with interpigment distances varying from 11 to 14 Å inside each unit (4). The complex mediates energy transfer pathways originating in the efficient natural solar energy antenna—the chlorosome, and ending at the energy conversion apparatus—the reaction center (5).

Steady-state optical spectra (absorption, linear dichroism), as well as time-resolved fluorescence and pump-probe signals, are well described by the Frenkel exciton model in conjunction with the Redfield equations for energy transport in the strong coupling limit (4–9). The complex absorption (Fig. 1 *b*) spans the 12,000–13,000 cm^{-1} energy region and in this exciton band, $\sim 1000 \text{ cm}^{-1}$ of energy dissipates within several picoseconds. The much longer excited-state lifetime (a few nanoseconds) allows the excitation to be transferred to the reaction center with high efficiency. Coherent one-dimensional photon echo (PE) measurements provided the first evidence of quantum coherences (7). Two-

dimensional (2D) PE spectroscopy has recently been applied to study the exciton transport pathways in FMO (8,9). A rich peak pattern of diagonal and off-diagonal features has been revealed. Simulations provided a good fit to experiment and the energy transfer through space was visualized using the exciton wavefunctions (8). Two energy transfer pathways were predicted by the simulations (Fig. 1 *a*, *green* and *red* arrows). However, these were not well resolved in the experiment due to spectral congestion. The 2D experiments also showed evidence of long-lived electronic quantum coherences (9).

The 2D PE signal (Fig. 1 *c*) is generated by applying three ultrashort laser pulses, with wavevectors \mathbf{k}_j and polarization directions \mathbf{v}_j ($j = 1, 2, 3$) (10). The signal is detected in the phase-matching direction $\mathbf{k}_S = -\mathbf{k}_1 + \mathbf{k}_2 + \mathbf{k}_3$; t_1 , t_2 , and t_3 are the time delays between pulses. 2D Fourier transforms of the signal amplitude with respect to the first and the third delay periods, $t_1 \rightarrow \Omega_1$ and $t_3 \rightarrow \Omega_3$ provide correlation plots for events occurring during t_1 and t_3 (Fig. 1 *d*). These are displayed for different values of the middle delay t_2 . Considerable effort has been devoted to developing methods for relating 2D PE signals to system properties (8–12). It is well established that the diagonal ($\Omega_1 = -\Omega_3$) peak positions correspond to excitation energies and their lineshapes show lifetimes and couplings to the environment. The crosspeaks ($\Omega_1 \neq -\Omega_3$) carry additional information about couplings and correlations of different states, which determine the energy-flow pathways and timescales.

METHODS

Optical properties of molecular aggregates are related to transition energies of individual chromophores and resonant couplings between them. The

Submitted October 10, 2007, and accepted for publication December 11, 2007.

Address reprint requests to Shaul Mukamel, 1102 Natural Sciences 2, University of California, Irvine, CA 92697-2025. Tel.: 949-824-6164; Fax: 949-824-8571; E-mail: smukamel@uci.edu.

Dmitri V. Voronine's present address is Physikalisches Institut, Universität Würzburg, Am Hubland, 97074 Würzburg, Germany.

Editor: Janos K. Lanyi.

© 2008 by the Biophysical Society
0006-3495/08/05/3613/07 \$2.00

doi: 10.1529/biophysj.107.123455

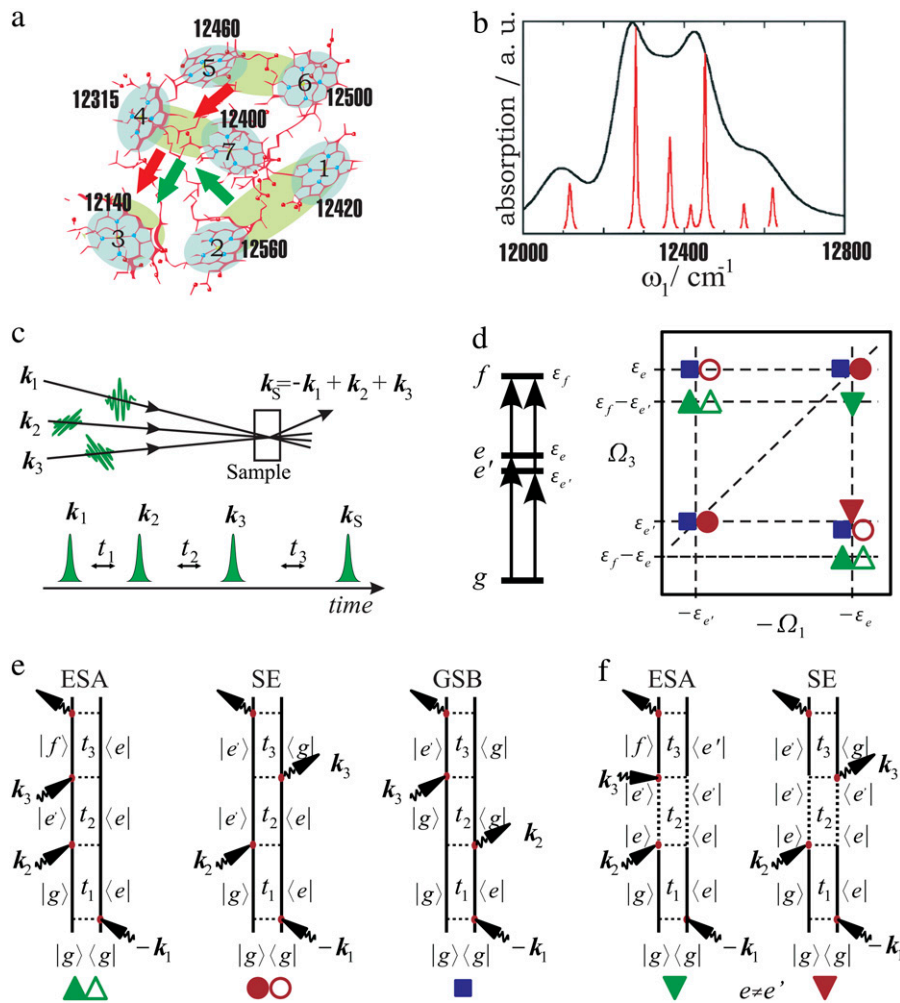


FIGURE 1 (a) Structure of the FMO complex, in which light blue areas show pigments (only pigment molecules (BChl) are shown); green areas indicate the extent of delocalized excitons, and arrows show predicted population relaxation pathways. (b) The simulated absorption spectrum (for model and parameters, see Methods). System energy levels and their oscillator strength are shown in red. (c) Scheme of the four-pulse time-domain experiment. t_1 , t_2 , and t_3 are the delays between pulses. Polarizations and wavevectors are the control parameters. (d) Energy-level scheme and the corresponding 2D PE spectrum of a dimer of two-level molecules. Solid and open symbols indicate contributions when the density matrix is diagonal (populations) and off-diagonal (coherences), respectively, during t_2 . (e and f) Feynman diagrams for 2D PE signal without population transport (energy dissipation). Symbols are as in d. (f) Additional diagrams, including exciton population relaxation with $e \neq e'$. The pathways are labeled ESA (excited-state absorption); SE (stimulated emission); and GSB (ground-state bleaching).

Frenkel exciton model provides a useful approximation for the system eigenstates and their optical properties. The Q_y band of FMO was described using the Hamiltonian of Aartsma as refined by Brixner et al. (5,8). Atomic coordinates were taken from Camara-Artigas et al. (3). The electric transition dipoles were assumed to pass through the nitrogen b and d atoms according to the crystallographic nomenclature. The monomer electric dipole strength was 28.7 D (2) (magnetic transition properties were neglected (3)). The coordinates of the magnesium atoms located at the center of BChl *a* molecules were used as the reference points of chromophore coordinates.

We have used the overdamped Brownian oscillator spectral density to represent the FMO complex coupling to the bath (11). The bath relaxation time was set to $\Lambda^{-1} = 100$ fs and the reorganization energy $\lambda = 55$ cm^{-1} of each BChl. These parameters were obtained from fits of the linear absorption spectrum, exciton relaxation timescales, and 2D PE spectrum at various time delays with *xxx* polarizations. In addition, we performed an ensemble averaging using a 500 snapshot sampling of the site energies with Gaussian disorder (variance is 20 cm^{-1} , as proposed by Brixner et al. (8)).

The third-order 2D PE signal was calculated using the sum-over-states expressions given in Zhang et al. (11). Their symmetry properties are deduced by calculating orientationally averaged amplitudes at various pathways. Orientationally averaging was calculated as described previously (13). The time evolution of the system density matrix during the three time intervals was described using the Redfield equations within the secular approximation for the system density-matrix evolution (11). The Redfield

equation, used during t_2 , then reduces to a Pauli master equation for diagonal density-matrix elements. Our analysis only holds within this model.

Exciton dynamics in the FMO complex

The two exciton relaxation pathways (Fig. 1 *a*) result in several distinct features in the 2D PE spectra: the easily distinguishable peaks related to the “green” and “red” relaxation pathways should appear after the relaxation at positions marked by circles of the same color in Fig. 2 *a*. Our calculated 2D PE signal of FMO with all pulse polarizations parallel (Fig. 2 *a* (xxx)) is dominated by strong diagonal peaks, as found experimentally. The spectra evolve with delay t_2 . However, the strong congestion makes it hard to assign the spectral patterns to specific states. Only one peak clearly fits the red circle, indicating a strong contribution from this pathway. The green pathway remains undetected. In this article, we demonstrate how additional dynamical information may be obtained by making use of a new set of control parameters—pulse polarizations. Elaborate pulse sequences are routinely used in the NMR to probe specific dynamical features of nuclear spins (14). We propose new optical pulse polarization configurations (PPC) designed to separate coherent and incoherent quantum evolution. Three levels of the pulse sequence design are presented by employing fundamental symmetries of the regular 2D PE signal and making use of the complex chirality.

What kind of quantum dynamics could be relevant for 2D photon echoes? The induced polarization vector, which is measured in 2D PE, reflects

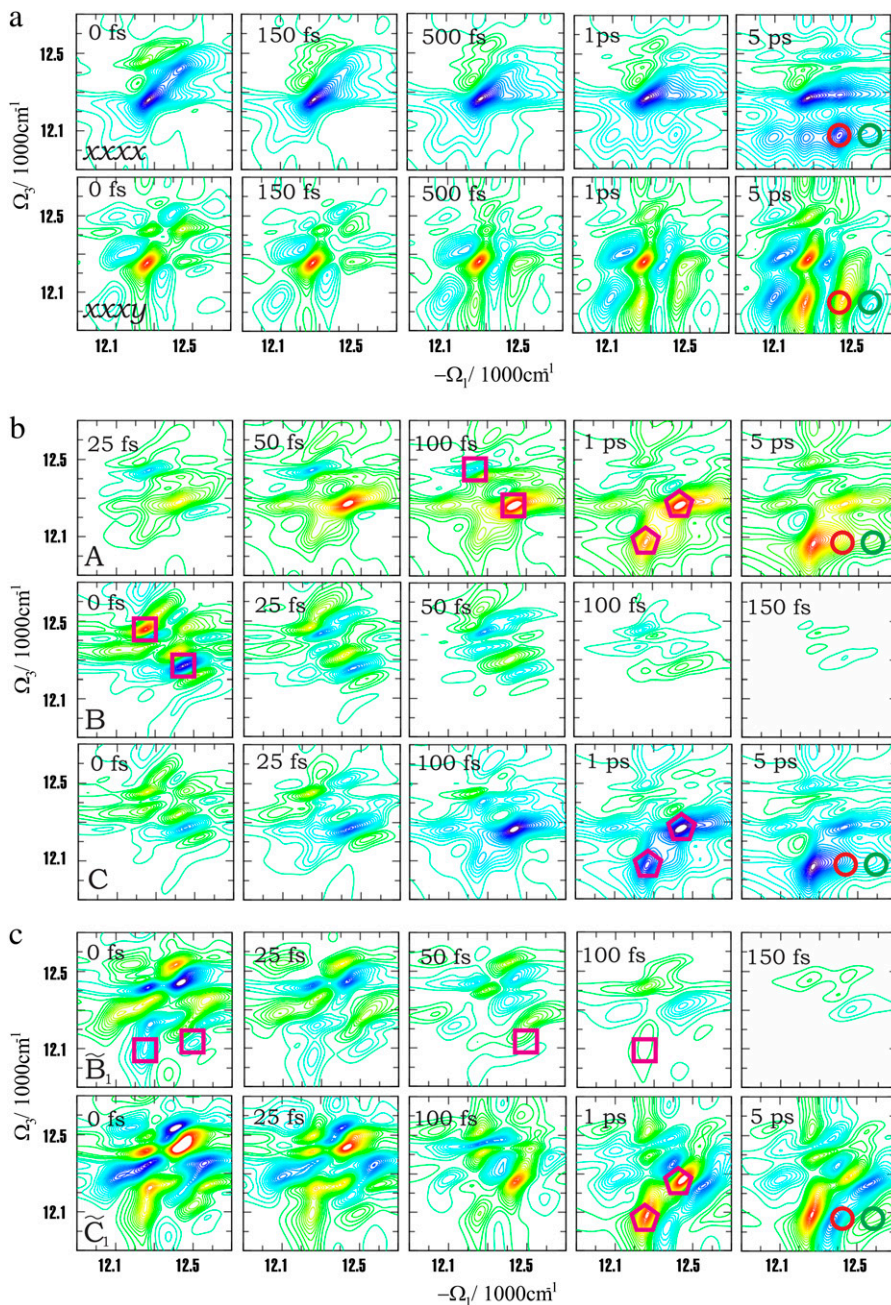


FIGURE 2 (a) Simulated 2D PE signals of the FMO complex: (upper row) xxxx nonchiral component; (lower row) xxxy(zzzz) chirality-induced component. (b) Simulated 2D PE signals of type A–C. A shows how the dynamics in t_2 breaks the $t_2 = 0$ symmetry, B reveals quantum oscillations of the density matrix, and C shows population relaxation (energy dissipation). (c) Simulated 2D PE chiral signals B_1 and C_1 for FMO: these signals reveal finer detail than B and C, respectively.

dynamical properties of the exciton density matrix during each of the time delays, t_1 , t_2 , and t_3 . These properties can be deduced with the help of the Feynman diagrams shown in Fig. 1, *e* and *f* (15). The signal is proportional to the response function $S^{(3)}$ given by a sum over all resonant pathways of the density matrix. These pathways represent sequences of intermediate states, which show up between the various interactions with the laser pulses. The contribution of pathway η to the signal may be represented as $S_{\eta}^{(3)} = M_{\eta} \times G_{\eta}(t_3, t_2, t_1)$, where M is a PPC geometry-dependent amplitude given by the transition dipole configuration and G represents the time dependence of excitons. We shall briefly describe M and G separately.

$G_{\eta}(t_3, t_2, t_1)$ contains all relevant system dynamics in pathway η , as can be deduced from the diagrams in Fig. 1, *e* and *f*: during t_1 the system experiences oscillations between the ground and the singly excited state e (frequency

$\sim 12,000 \text{ cm}^{-1}$ for FMO—these are interband frequencies). During delay t_2 , only intraband frequency oscillations ($0\text{--}800 \text{ cm}^{-1}$) show up. These correspond to coherent oscillations between two singly excited states or populations. Population relaxation and transport take place as well. Interband oscillations are again observed during t_3 (these also include interband one- to two-exciton frequencies). Fourier transforms with respect to t_1 and t_3 translate the interband oscillations into resonant peaks. Excited-state evolution can be directly followed by comparing the 2D peak patterns for various t_2 . To give some insight into how this works, in Fig. 1 *d* we sketch the 2D PE signal of a simplified model dimer of two-level chromophores which has two one-exciton energy levels and a single two-exciton level. The spectrum at finite t_2 contains contributions from all diagrams, as indicated by the graphic symbols.

The amplitude M can be controlled by PPC and has fundamental symmetry properties, i.e., it is invariant to certain permutations of PPC. We employ these to construct optimal PPCs that control the signals and highlight desired features. First, we notice that when the delay time t_2 in Fig. 1 *c* is set to 0, the signal must be invariant to exchange of the second and third pulses, since they are indistinguishable. This implies permutation symmetry of the wavevectors and polarizations of these two pulses at $t_2 = 0$. This symmetry can be verified by noting that at $t_2 = 0$, the permutation interchanges the stimulated emission (SE) and ground-state bleaching (GSB) diagrams and does not affect excited-state absorption (ESA), leaving the total response function intact (the notation is introduced in Fig. 1, *e* and *f*).

As quantum dynamics sets in for $t_2 > 0$, this symmetry breaks down. Three symmetry-breaking mechanisms of M can be identified. These affect SE and ESA pathways (GSB does not evolve during t_2). 1), Coherent evolution of the phase $\varphi = \omega_{ee'}$ of the density matrix is inherent to multilevel systems and takes place on the τ_E timescale (the inverse one-exciton manifold bandwidth). 2), Decays of density-matrix coherences during t_2 on the pure dephasing timescale τ_d . 3), Incoherent transport (population relaxation) is observed on the τ_p timescale.

Pulse-design strategies

Level 1: displaying symmetry breaking

As the first level of pulse design, we use the three independent PPCs for isotropic systems in the dipole approximation (13) and introduce the signal $A \equiv S_{xyxy}^{(3)}(\Omega_3, t_2, \Omega_1) - S_{xyyx}^{(3)}(\Omega_3, t_2, \Omega_1)$, where the subscript indicates the PPC as pulse-polarization directions $\nu_4\nu_3\nu_2\nu_1$. This signal must vanish identically at $t_2 = 0$ due to the above described symmetry, and will gradually build up, with t_2 showing coherent evolution, dephasing, and transport. The signal A thus highlights dynamical features of the spectra: static features, which cancel by symmetry at $t_2 = 0$, are eliminated. If the timescales are well separated, $\tau_E < \tau_d < \tau_p$, the coherent evolution will show up on the shortest timescale and will result in oscillating crosspeaks due to the oscillating pattern of the density-matrix coherent evolution. The dephasing mechanism will subsequently appear during τ_d through a gradual decay of crosspeak oscillation magnitude at longer times. Population transport will induce a large asymmetry of SE-related crosspeaks within τ_p . For our model dimer in Fig. 1 *d*, the signal A at $t_2 \approx \tau_E$ will only show oscillating crosspeaks due to open symbols (diagonal peaks will cancel!); at $t_2 \approx \tau_d$, the oscillations will decay and the stationary crosspeaks will develop due to the GSB and ESA; at $t_2 \approx \tau_p$, the higher-energy diagonal peak at e_c will develop due to population relaxation from state e to e' , together with inverted triangles (the solid circle with solid triangle, both corresponding to the higher-energy state e , will disappear).

The three permutation symmetry-breaking processes described above can thus be visualized using the A signal shown in Fig. 2 *b*. Here, the relevant timescales τ_E , τ_d , and τ_p are 50–100 fs, 20–50 fs, and 500 fs to 5 ps, respectively. The signal vanishes at $t_2 = 0$ and rapidly builds up within 50 fs. We observe a complicated 100-fs dynamics: fine details of the spectrum evolve rapidly. Some peaks grow up and decay, whereas other peaks steadily grow and survive up to 1 ps. At 5 ps, the peak amplitudes redistribute again (this is different from the ordinary $xxxx$ spectra, which hardly change earlier than 1 ps). Four peaks can be identified. They are marked by squares (symmetric with respect to the diagonal line) and pentagons, which redistribute at long times. We also note that one square (100 fs) and one pentagon (1 ps) appear at the same position. Although the short-time behavior could be attributed to coherent evolution and the long-time dynamics to incoherent population relaxation, this cannot be unambiguously inferred from these signals, since the times τ_E and τ_d are not well separated. It is therefore difficult to distinguish between the three symmetry-breaking mechanisms from the signal A alone.

Level 2: separating coherent and incoherent dynamics

Can one distinguish between these processes using some additional symmetries? To address this question, we need to examine other properties of the

pathways and search for specific signatures of populations and coherences. The pathways η may be classified according to whether the state of the system during t_2 is a population (population pathways, η_{pp}) or a coherence (coherent pathways, η_{cp}). These are represented respectively by diagonal (ρ_{ee}) and off-diagonal ($\rho_{ee'}$, $e \neq e'$) exciton density-matrix elements. The solid symbols in Fig. 1 *d* indicate contributions from population pathways, and the open symbols contributions from coherence pathways.

As can be seen in Fig. 1, *e* and *f*, a common feature of all population pathways is that the first two interactions induce the same transition, $\alpha = l$ (doorway). The last two interactions induce the same transition, too, $\alpha = w$ (window). The amplitudes of this set of interactions, $M_{\eta_{pp}}$, for isotropic systems are given in the Appendix. The key point is that the population pathways have the symmetry $M_{\eta_{pp}}(xyyx) = M_{\eta_{pp}}(xyxy)$ for an arbitrary delay t_2 (here, the PPC is denoted by $M(\nu_4\nu_3\nu_2\nu_1)$).

Another set of pathways can be isolated by inspecting the coherent contribution to SE, defined by the SE diagram in Fig. 1 *e*. We find that these pathways are characterized by only two optical transitions: the first and the third transitions on the righthand side of the diagram are identical, $\alpha = r$, whereas the second and fourth transitions on the lefthand side of the diagram are also identical, $\alpha = l$ (we note that this property is valid for density-matrix coherences ($\rho_{ee'}$) and populations (ρ_{ee}) during t_2 ; however, all such SE pathways are coherent, since they do not involve energy dissipation). By calculating the pathway amplitude we find an additional symmetry $M_{\eta_{cp}}(xyyx) = M_{\eta_{cp}}(xyxy)$ (other amplitudes are given in the Appendix).

Exploiting these new symmetries, in the second level of pulse design, we propose the combination $B \equiv S_{xyxy}^{(3)}(\Omega_3, t_2, \Omega_1) - S_{xyyx}^{(3)}(\Omega_3, t_2, \Omega_1)$ to cancel population signatures and to display coherent quantum dynamics, and $C \equiv S_{xyxy}^{(3)}(\Omega_3, t_2, \Omega_1) - S_{xyyx}^{(3)}(\Omega_3, t_2, \Omega_1)$ to cancel SE coherent pathway contributions and thus highlight the remaining population contributions. The B signal can be interpreted as follows: only coherent t_2 dynamics will be seen by the coherence pathways. For our model dimer in Fig. 1 *d*, all solid symbols will thus be eliminated in B , and the open symbols from ESA and SE with density-matrix coherences will remain. The C signal will eliminate the SE coherent pathways: these overlap with population pathways (ESA coherent peaks along Ω_3 that reflect double-exciton resonances are shifted from these crosspeaks when the two-exciton-state energy is different from $\epsilon_c + \epsilon_{c'}$). Population relaxation during t_2 can be monitored through the redistribution of crosspeak amplitudes. In Fig. 1 *d*, the C signal eliminates the open and solid red circles at all t_2 . By examining the GSB diagram, we find that blue squares at the diagonal will also be eliminated. Thus, in the C signal, the population contribution (*solid inverted triangles*) will clearly show up, with no background from the coherent pathways. It should also be noted that B and C signals cancel contributions with $d = w$ and $l = r$, respectively; the diagonal peaks will also be eliminated in both signals at $t_2 = 0$.

The signal B of FMO displayed in Fig. 2 *b* shows a remarkable anti-diagonal distribution of peaks indicating coherent dynamics. The peaks evolve within 100 fs and decay in 150 fs. Oscillations with their characteristic frequencies (~ 100 – 300 cm^{-1} , corresponding to ~ 60 – 20 fs) can be observed. The squares indicate the same peaks as in A : here, they change signs in 100 fs. The 2D spectra vanish in 200 fs. The signals C in Fig. 2 *b* show the population pathways; the growth of peaks reflects the population redistribution. From the B signals, we deduce that coherences decay within 150 fs, assuring that the C signals show only population transfer after 100 fs. The rise and fall of crosspeaks reflect these phenomena: the crosspeaks (pentagons) provide a clear indication of population redistribution. This level of detail is not offered by the simple 2D PE ($xxxx$) configuration due to spectral congestion.

Level 3: employing chiral sensitivity

A third level of pulse design is achieved by making use of the chirality of complex geometry. Chirality-induced (CI) 2D PE polarization configurations (13) constitute a nonlinear extension of the circular dichroism (CD) (16), which is widely used for structure determination. The nonlinear optical CI signals vanish in nonchiral systems and in racemic mixtures, and can improve the resolution of the 2D PE signals (13). A typical 2D PE CI signal

($xxxy$) simulated for the FMO complex is shown in Fig. 2 *a*. It reveals many additional features not resolved in the ($xxxx$) spectra, where the weak crosspeaks have the same signs and overlap with the diagonal peaks. A finer pattern is achieved due to the alternating signs and stronger crosspeaks induced by the chiral geometry. Two crosspeaks, circled in red and green in Fig. 2 *a* ($xxxy$) at 5 ps, are now clearly visible, revealing both population relaxation pathways depicted in Fig. 1 *a*. Numerous additional features are also visible: these carry a wealth of information. Further theoretical analysis is required for their interpretation.

By exploiting the CI signal symmetries we developed specific chirality-sensitive extensions of the A , B , and C signals. These will be denoted \tilde{A} , \tilde{B} , and \tilde{C} , respectively. We found three possible PPCs for each signal. These are listed in the Appendix. Here, we present one example of each type: $\tilde{B}_1 \equiv S_{xyz(n)}^{(3)}(\Omega_3, t_2, \Omega_1) - S_{xyz(n)}^{(3)}(\Omega_3, t_2, \Omega_1)$, and $\tilde{C}_1 \equiv S_{xyz(n)}^{(3)}(\Omega_3, t_2, \Omega_1) - S_{xyz(n)}^{(3)}(\Omega_3, t_2, \Omega_1)$, where (n) denotes a noncollinear and (c) a collinear laser configuration. For our model dimer, these signals will eliminate the same peaks as in B and C , respectively, but each peak will have an additional fine structure associated with chirality.

The \tilde{B}_1 and \tilde{C}_1 signals displayed in Fig. 2 *c* show very different patterns from their nonchiral counterparts. A large number of new coherence peaks are observed in \tilde{B}_1 : crosspeaks that were not well resolved in B are clearly seen (Fig. 2 *c*, *squares*). In addition, we observe peak oscillations with different frequencies: one changes sign in 50 fs, whereas the other does so in 100 fs. This gives the energy difference of the eigenstates involved in this coherence. The signal \tilde{C}_1 also shows many more features than the C . Peaks originating from different chiral regions now have distinct peak color (sign) and peak assignment becomes much easier. The rise of the crosspeaks attributed to two distinct population pathways (Fig. 2 *c*, *red and green circles*) is clearly visible in the \tilde{C}_1 signal, and intermediate stages along the relaxation pathways can be easily monitored through the growth and decay of crosspeak amplitudes.

DISCUSSION

This article presents novel ways for analyzing multidimensional optical signals and extracting the underlying dynamics in ensembles of randomly oriented multilevel quantum systems. Simplifying such signals by eliminating diagonal peaks using specific polarization configurations has been used in the infrared for structure determination (12). By exploiting the spectral symmetries, we obtain specific probes of coherent and incoherent excitation dynamics. Apart from eliminating diagonal peaks, the family of B signals further cancels the contributions of population pathways altogether (both diagonal and off diagonal). These signals therefore only reveal coherent quantum dynamics during t_2 . The C signals show incoherent relaxation. A chirality fingerprint is an important refinement that provides a much richer dynamical pattern by enhancing fine details. Developing direct relations between the underlying chiral structure and the spectra remains an open challenge.

The proposed signals are based on the assumption that each optical pulse interacts only once with the system and that the pulses are temporally well separated. In addition, they are short compared to the exciton and bath dynamics timescale (i.e., impulsive) and their bandwidth covers the entire exciton band. In this regime the signals are directly given by the response function. Including a finite bandwidth of nonimpulsive excitations may be necessary for realistic simulations. These corrections will be small when exciton

coherent dynamics is maintained within the pulse. From Fig. 2, the coherent regime lasts for 200 fs and coherent exciton oscillations have an ~ 60 - to 100-fs period. Pulses of 50 fs ($\sim 1000 \text{ cm}^{-1}$ bandwidth) used in the recent experiments (8,9) will thus be impulsive for the FMO complex. Closed expressions that include finite pulse envelopes were derived by Schweigert and Mukamel (17) and may be used when necessary. These generalized expressions may be used to apply pulse-shaping techniques for simplifying the signals (18).

The proposed signals have many applications beyond photosynthesis. For instance, coherent quantum dynamics, as revealed by the B signals, is especially important for quantum computing, where the detection, manipulation, and preservation of pure states by minimizing decoherence is an important goal (19). The signal B tags pure states and decays with the decoherence timescale. Therefore, the evolution of pure states can be visualized by our proposed signals. The interplay of coherent motion and incoherent dissipation is essential for the inner working of molecular motors. Two-dimensional vibrational spectra of molecular switches have been reported (20).

APPENDIX

Here we present a derivation of the amplitudes of coherent and population pathways in isotropic systems.

Population pathways in nonchiral and chiral PPCs

In the dipole approximation, the response function is a fourth-rank tensor with respect to field polarizations: $S^{(3)} \equiv S_{\nu_4 \nu_3 \nu_2 \nu_1}^{(3)}$, where $\nu_j = x, y, z$ is the lab-frame polarization direction of the incoming pulses $j = 1, 2, 3$ and the signal $j = 4$. These tensor properties enter through the pathway amplitudes $M_\eta \equiv M_\eta(\nu_4 \nu_3 \nu_2 \nu_1)$. For a molecule whose orientation is fixed in the lab frame, the amplitude of the population pathway is $M_{\eta_{pp}} = \mu_w^{\nu_4} \mu_w^{\nu_3} \mu_d^{\nu_2} \mu_d^{\nu_1}$, where μ_α^ν is the ν th component of the transition dipole of the α transition. For an ensemble of randomly oriented molecules, the orientationally averaged amplitudes $M_{\eta_{pp}} = \langle \mu_w^{\nu_4} \mu_w^{\nu_3} \mu_d^{\nu_2} \mu_d^{\nu_1} \rangle$ are needed. These averagings have been calculated using the tensor expressions given in Abramavicius et al. (13). Due to spherical symmetry, many tensor components vanish in isotropic systems, whereas others are linearly dependent. Obviously, $\nu_4 \nu_3 \nu_2 \nu_1 = xxxx$ is the same as $yyyy$ and $zzzz$. There are only three independent PPCs: $\nu_4 \nu_3 \nu_2 \nu_1 = xxyy$, $xyxy$, and $xyyx$.

The ensemble-averaged amplitudes of the population pathways characterized by d and w transitions are

$$M_{\eta_{pp}}(xxyy) = \frac{2}{30}(2\mu_w^2 \mu_d^2 - (\mu_w \cdot \mu_d)^2)$$

$$M_{\eta_{pp}}(xyxy) = M_{\eta_{pp}}(xyyx) = \frac{1}{30}(-\mu_w^2 \mu_d^2 + 3(\mu_w \cdot \mu_d)^2).$$

Chirality-specific configurations are calculated to first order in the optical wavevector. The response function is no longer a fourth-rank tensor, since it depends parametrically also on the field wavevectors, \mathbf{k}_j : $S^{(3)} \equiv S_{\Phi_4 \Phi_3 \Phi_2 \Phi_1}^{(3)}$, where $\Phi \equiv (\mathbf{k}, \nu)$. However, when all four wavevector magnitudes are similar (as is typically the case in resonant spectroscopy of excitons), we can decompose the wavevectors in the lab frame, $\mathbf{k}_j \equiv x\mathbf{k}_j^x + y\mathbf{k}_j^y + z\mathbf{k}_j^z$. The response function is then given by four fifth-rank tensors, where the wavevector direction coincides with one of the coordinate axes. The pathway amplitudes can then be written as

$$M_{\eta}(\nu_4\nu_3\nu_2\nu_1; \kappa_4\kappa_3\kappa_2\kappa_1) = \frac{2\pi}{\lambda} [\bar{M}_{\eta}^{(4)}(\nu_4\nu_3\nu_2\nu_1\kappa_4) + \bar{M}_{\eta}^{(3)}(\nu_4\nu_3\nu_2\nu_1\kappa_3) + \bar{M}_{\eta}^{(2)}(\nu_4\nu_3\nu_2\nu_1\kappa_2) + \bar{M}_{\eta}^{(1)}(\nu_4\nu_3\nu_2\nu_1\kappa_1)].$$

κ_j is now the direction of the j th pulse wavevector and λ is the mean wavelength; $\bar{M}_{\eta}^{(j)}(\nu_4\nu_3\nu_2\nu_1\kappa_j)$ is the fifth-rank tensor with respect to all pulse polarizations and the j th pulse wavevector direction. In the following, we will use the notation $M_{\eta}(\nu_4\nu_3\nu_2\nu_1; \kappa_4\kappa_3\kappa_2\kappa_1) \equiv M_{\eta}(\nu_4\nu_3\nu_2\nu_1; c/n)$, where c will stand for collinear and n for noncollinear laser configurations (these are easily deduced from Crabtree and Lewis (1)). Upon orientational averaging of fifth-rank tensors, we found nine independent chirality-induced PPCs. An arbitrary chirality-induced field configuration may then be described as a linear combination of these nine components.

In CI signals, the transition α can be mediated either by the transition dipole μ_{α} or by the transition quadrupole q_{α} . The amplitudes for the population pathways in the nine independent CI PPCs are

$$\begin{aligned} M_{\eta_{pp}}(xyzx; n) &= \frac{2\pi}{30\lambda} (2\xi_{dw}^{(1)} - \xi_{dw}^{(2)} + \xi_{dw}^{(3)} + \xi_{wd}^{(1)} + \xi_{wd}^{(4)}) \\ M_{\eta_{pp}}(xyxz; n) &= M_{\eta_{pp}}(yxzx; n) \\ M_{\eta_{pp}}(xyxx; c) &= \frac{4\pi}{30\lambda} (-2\xi_{dw}^{(1)} + \xi_{dw}^{(2)} - 3\xi_{dw}^{(3)} + \xi_{dw}^{(4)}) \\ M_{\eta_{pp}}(xyxx; n) &= M_{\eta_{pp}}(xyxx; c) \\ M_{\eta_{pp}}(xxyz; n) &= \frac{4\pi}{30\lambda} (-3\xi_{wd}^{(1)} + \xi_{wd}^{(2)} + \xi_{wd}^{(4)}) \\ M_{\eta_{pp}}(xxyx; c) &= \frac{4\pi}{30\lambda} (\xi_{dw}^{(1)} - \xi_{dw}^{(2)} + \xi_{dw}^{(3)} - \xi_{dw}^{(4)} + \xi_{wd}^{(1)} - 2\xi_{wd}^{(2)} - 2\xi_{wd}^{(4)}) \\ M_{\eta_{pp}}(xxyx; n) &= \frac{2\pi}{30\lambda} (\xi_{dw}^{(1)} + \xi_{dw}^{(3)} - 2\xi_{dw}^{(4)} + \xi_{wd}^{(1)} - \xi_{wd}^{(2)} - 3\xi_{wd}^{(4)}) \\ M_{\eta_{pp}}(xxxy; c) &= \frac{4\pi}{30\lambda} (\xi_{dw}^{(1)} - \xi_{dw}^{(2)} + \xi_{dw}^{(3)} - \xi_{dw}^{(4)} - \xi_{wd}^{(1)} + 2\xi_{wd}^{(2)} + 2\xi_{wd}^{(4)}) \\ M_{\eta_{pp}}(xxxy; n) &= M_{\eta_{pp}}(xxxy; c), \end{aligned}$$

where we have defined (13)

$$\begin{aligned} \xi_{\alpha\beta}^{(1)} &= \mu_{\alpha} \cdot q_{\beta} \cdot \mu_{\alpha} \cdot \mu_{\beta} \\ \xi_{\alpha\beta}^{(2)} &= \mu_{\alpha} \cdot \mu_{\beta} \cdot q_{\beta} \cdot \mu_{\alpha} \\ \xi_{\alpha\beta}^{(3)} &= \mu_{\beta} \circ q_{\beta} \mu_{\alpha}^2 \\ \xi_{\alpha\beta}^{(4)} &= \mu_{\alpha} \circ q_{\beta} \mu_{\beta} \cdot \mu_{\alpha}. \end{aligned}$$

SE coherent pathways

For nonchiral techniques, the amplitudes of SE coherent pathways are

$$\begin{aligned} M_{\eta_{cp}}(xxyy) &= M_{\eta_{cp}}(xyyx) = \frac{1}{30} (-\mu_i^2 \mu_r^2 + 3(\mu_i \cdot \mu_r)^2) \\ M_{\eta_{cp}}(xyxy) &= \frac{2}{30} (2\mu_i^2 \mu_r^2 - (\mu_i \cdot \mu_r)^2). \end{aligned}$$

For CI techniques, we get

$$\begin{aligned} M_{\eta_{cp}}(xyzx; n) &= \frac{2\pi}{30\lambda} (2\xi_{nl}^{(1)} - \xi_{nl}^{(2)} + \xi_{nl}^{(3)} + \xi_{lr}^{(1)} - \xi_{lr}^{(4)}) \\ M_{\eta_{cp}}(xyxz; n) &= \frac{4\pi}{30\lambda} (-3\xi_{lr}^{(1)} + \xi_{lr}^{(2)} + \xi_{lr}^{(4)}) \\ M_{\eta_{cp}}(xyxx; c) &= \frac{4\pi}{30\lambda} (\xi_{nl}^{(1)} - \xi_{nl}^{(2)} + \xi_{nl}^{(3)} - \xi_{nl}^{(4)} + \xi_{lr}^{(1)} - 2\xi_{lr}^{(2)} - 2\xi_{lr}^{(4)}) \\ M_{\eta_{cp}}(xyxx; n) &= \frac{2\pi}{30\lambda} (\xi_{nl}^{(1)} + \xi_{nl}^{(3)} - 2\xi_{nl}^{(4)} + \xi_{lr}^{(1)} - \xi_{lr}^{(2)} - 3\xi_{lr}^{(4)}) \\ M_{\eta_{cp}}(xxyz; n) &= M_{\eta_{cp}}(xyzx; n) \\ M_{\eta_{cp}}(xxyx; c) &= \frac{4\pi}{30\lambda} (-2\xi_{nl}^{(1)} + \xi_{nl}^{(2)} + \xi_{nl}^{(4)} + 3\xi_{lr}^{(2)}) \\ M_{\eta_{cp}}(xxyx; n) &= M_{\eta_{cp}}(xxyx; c) \\ M_{\eta_{cp}}(xxxy; c) &= \frac{4\pi}{30\lambda} (\xi_{nl}^{(1)} - \xi_{nl}^{(2)} + \xi_{nl}^{(3)} - \xi_{nl}^{(4)} - \xi_{lr}^{(1)} + 2\xi_{lr}^{(2)} + 2\xi_{lr}^{(4)}) \\ M_{\eta_{cp}}(xxxy; n) &= M_{\eta_{cp}}(xyxx; n). \end{aligned}$$

CI extensions of A, B, and C signals

Based on the calculated peak amplitudes for coherence and population pathways, we design the following signals, which are induced by chirality:

$$\begin{aligned} \bar{A}_1 &= S_{xxyx(c)}^{(3)} - S_{xyxx(c)}^{(3)}, \quad \bar{A}_2 = S_{xxyx(n)}^{(3)} - S_{xyxx(n)}^{(3)}, \quad \bar{A}_3 = S_{xxyz(n)}^{(3)} - S_{xyxz(n)}^{(3)}, \\ \bar{B}_1 &= S_{xyxz(n)}^{(3)} - S_{xyxz(n)}^{(3)}, \quad \bar{B}_2 = S_{xyxx(c)}^{(3)} - S_{xyxx(n)}^{(3)}, \quad \bar{B}_3 = S_{xxyx(n)}^{(3)} - S_{xxyx(n)}^{(3)}, \\ \bar{C}_1 &= S_{xxyz(n)}^{(3)} - S_{xyxz(n)}^{(3)}, \quad \bar{C}_2 = S_{xxyx(n)}^{(3)} - S_{xxyx(c)}^{(3)}, \quad \bar{C}_3 = S_{xxyx(n)}^{(3)} - S_{xxyx(n)}^{(3)}. \end{aligned}$$

We thank Dr. Wei Zhuang for many useful discussions.

This research was supported by the National Institutes of Health (GM59230) and the National Science Foundation (CHE-0446555).

REFERENCES

- Crabtree, G. W., and N. S. Lewis. 2007. Solar energy conversion. *Phys. Today*. 60:37–42.
- Olson, J. 2004. The FMO protein. *Photosynth. Res.* 80:181–187.
- Camara-Artigas, A., R. Blankenship, and J. P. Allen. 2003. The structure of the FMO protein from *Chlorobium tepidum* at 2.2 Å resolution. *Photosynth. Res.* 75:49–55.
- van Amerongen, H., L. Valkunas, and R. van Grondelle. 2000. *Photosynthetic Excitons*. World Scientific, Singapore.
- Vulto, S. I. E., M. A. de Baat, S. Neerken, F. R. Nowak, H. van Amerongen, J. Amesz, and T. J. Aartsma. 1999. Excited state dynamics of in FMO antenna complexes from photosynthetic green sulphur bacteria: a kinetic model. *J. Phys. Chem. B.* 103:8153–8161.
- Adolphs, J., and T. Renger. 2006. How proteins trigger excitation energy transfer in the FMO complex of green sulphur bacteria. *Biophys. J.* 91:2778–2797.
- Prokhorenko, V. I., A. R. Holzwarth, F. R. Nowak, and T. J. Aartsma. 2002. Growing-in of optical coherence in the FMO antenna complexes. *J. Phys. Chem. B.* 106:9923–9933.

8. Brixner, T., J. Stenger, H. M. Vaswani, M. Cho, R. E. Blankenship, and G. R. Fleming. 2005. Two-dimensional spectroscopy of electronic couplings in photosynthesis. *Nature*. 434:625–628.
9. Engel, G. S., T. R. Calhoun, E. L. Read, T. K. Ahn, T. Man, Y. C. Cheng, R. E. Blankenship, and G. R. Fleming. 2007. Evidence of wavelike energy transfer through quantum coherence in photosynthetic systems. *Nature*. 446:782–786.
10. Mukamel, S. 2000. Multidimensional femtosecond correlation spectroscopies of electronic and vibrational excitations. *Annu. Rev. Phys. Chem.* 51:691–729.
11. Zhang, W. M., T. Meier, V. Chernyak, and S. Mukamel. 1998. Exciton-migration and three-pulse femtosecond optical spectroscopies of photosynthetic antenna complexes. *J. Chem. Phys.* 108:7763–7774.
12. Zanni, M. T., N. H. Ge, Y. S. Kim, and R. M. Hochstrasser. 2001. Two-dimensional IR spectroscopy can be designed to eliminate the diagonal peaks and expose only the crosspeaks needed for structure determination. *Proc. Natl. Acad. Sci. USA*. 98:11265–11270.
13. Abramavicius, D., W. Zhuang, and S. Mukamel. 2006. Probing molecular chirality via excitonic nonlinear response. *J. Phys. B Atom. Mol. Opt. Phys.* 36:5051–5066.
14. Ernst, R. R., G. Bodenhausen, and A. Wokaun. 1998. Principles of Nuclear Magnetic Resonance in One and Two Dimensions. Clarendon Press, Oxford, UK.
15. Mukamel, S. 1995. Principles of Nonlinear Optical Spectroscopy. Oxford University Press, New York.
16. Berova, N., K. Nakanishi, and R. W. Woody, editors. 2000. Circular Dichroism. Principles and Applications 2nd ed. John Wiley & Sons, New York.
17. Schweigert, I. V. and S. Mukamel. 2008. Simulating multidimensional optical wave mixing signals with finite pulse envelopes. *Phys. Rev. A*. 77:033802.
18. Voronine, D., D. Abramavicius, and S. Mukamel. 2007. Manipulating multidimensional electronic spectra of excitons by polarization pulse shaping. *J. Chem. Phys.* 126:044508.
19. Nielsen, M. A., and I. L. Chuang. 2001. Quantum Computation and Quantum Information. Cambridge University Press, Cambridge, UK.
20. Larsen, O. F. A., P. Bodis, W. J. Buma, J. S. Hannam, D. A. Leigh, and S. Woutersen. 2005. Probing the structure of rotaxane with two-dimensional infrared spectroscopy. *Proc. Natl. Acad. Sci. USA*. 102:13378–13382.